Reconstruction in interferometric synthetic aperture microscopy: comparison with optical coherence tomography and digital holographic microscopy

Colin R. J. Sheppard,[1,2,3] Shan Shan Kou,[4] and Christian Depeusinge[4]

[1]*Optical Bioimaging Laboratory, Division of Bioengineering, National University of Singapore, Singapore 117574*
[2]*Department of Biological Sciences, National University of Singapore, Singapore 117543*
[3]*Singapore–MIT Alliance for Research and Technology (SMART), Singapore 117543*
[4]*Advanced Photonics Laboratory, Ecole Polytechnique Fédérale de Lausanne (EPFL), CH-1015 Lausanne, Switzerland*
**Corresponding author: colin@nus.edu.sg*

Received September 9, 2011; revised November 13, 2011; accepted November 13, 2011;
posted November 16, 2011 (Doc. ID 154444); published February 9, 2012

It is shown that the spatial frequencies recorded in interferometric synthetic aperture microscopy do not correspond to exact backscattering [as they do in unistatic synthetic aperture radar (SAR)] and that the reconstruction process based on SAR is therefore based on an approximation. The spatial frequency response is developed based on the three-dimensional coherent transfer function approach and compared with that in optical coherence tomography and digital holographic microscopy.

OCIS codes: 090.0090, 170.4500, 180.1790, 180.3170, 180.6900.

1. INTRODUCTION

Interferometric synthetic aperture microscopy (ISAM) is a promising technique for imaging into biological tissue, with widespread potential applications in both biology and clinical diagnosis [1–6]. It represents a significant improvement over conventional optical coherence tomography (OCT) [7] image reconstruction when the system aperture is large. Descriptions of ISAM present it as a combination of OCT and synthetic aperture radar. But the theory behind its operation, and why it works, is not completely apparent from the published papers. Here we describe the similarities and differences between ISAM and other techniques {OCT, optical coherence microscopy (OCM) [8], full-field OCT (FFOCT) [9–11], confocal interferometry [12], and digital holographic microscopy (DHM) [13–17]} using the framework of the coherent transfer function. The aim is to put ISAM on a strong theoretical foundation and to explore the advantages of the different methods and their optical implementation.

2. HOLOGRAPHIC MICROSCOPY

We start with considering DHM. Of course holography is basically interferometry. What makes it holography could be recognized as the reconstruction process, nowadays usually performed digitally. Holography can be performed in the Fresnel regime, but image plane holograms can also be generated [16]. An analysis of the three-dimensional (3D) imaging properties of holography was presented many years ago by Wolf [18]. An incident planar wave, with wave vector $\mathbf{k}_1$, is scattered by the object, which can be considered as a superposition of 3D gratings oriented in different directions. As the wavelength of the scattered wave, with wave vector $\mathbf{k}_2$, is the same as that of the illuminating wave, the grating vector $\mathbf{K} = K_x\mathbf{i} + K_y\mathbf{j} + K_z\mathbf{k}$ must necessarily lie on the surface of a sphere in K-space, radius $|\mathbf{k}_1| = |\mathbf{k}_2| = k$, passing through the origin. This sphere is called the Ewald sphere, after the construction in x-ray diffraction. The result is that only a very limited range of 3D spatial frequencies of the object is imaged: we can introduce a coherent transfer function (CTF), $c(\mathbf{K})$, which is zero everywhere except on the surface of the sphere. But another consequence is that, during the reconstruction process, the hologram can be refocused at any focal distance from a single hologram [19,20]. Wolf did not give any diagrams to illustrate his results, but Dändliker and Weiss presented figures to show how the Ewald sphere rotates with the direction of illumination [21]. Taking the illuminating wave to be traveling in the z direction, the equation of the sphere is $K_x^2 + K_y^2 + (K_z + k)^2 = k^2$, so that

$$K_z = -k \pm \sqrt{k^2 - K_x^2 - K_y^2}. \tag{1}$$

The two roots of Eq. (2) correspond to transmission and reflection geometry, respectively. Sheppard gave figures showing the form of the CTF for these cases [22]. If the object's scattering potential is $T(\mathbf{K})$, the 3D image amplitude is the inverse Fourier transform of the product $c(\mathbf{K})T(\mathbf{K})$ [23,24]. By the projection/slice theorem, the image amplitude at a particular plane z is given by the projection in the K_z direction of $\exp(iK_z z)c(\mathbf{K})T(\mathbf{K})$. The refocusing process in holographic reconstruction can be understood in terms of a propagation of the angular spectrum. Measurement of the image amplitude in any plane can be mapped on to the surface of the Ewald sphere and projected back into any plane using the projection slice theorem. The projection process is often performed by Fresnel diffraction theory, which approximates the Ewald sphere to a paraboloid of revolution (a different paraboloid for transmission or reflection geometry). Measurement of the hologram on different planes does not lead to any additional information. A range of wavelengths can, however,

be then used to sweep out a region of K-space, from which a 3D image can be reconstructed [17,20]. This is multiple-wavelength DHM, or MWDHM.

3. INTERFERENCE MICROSCOPES

A very general expression was given by Sheppard and Wilson for image formation in the general class of scanning interference microscopes [25]. In particular, this can be applied to both confocal interference microscopes and correlation microscopes. In a confocal microscope (which uses a detector pinhole), the effective CTF is given by the convolution $P_1 \otimes P_2$ of the pupil functions of the illuminating and collection lenses. This holds for the case of two-dimensional (2D) pupils but also gives the 3D CTF for the 3D case, using the 3D (generalized) pupil (a cap of a sphere) for P_1, P_2. The concept of the generalized pupil was introduced by McCutchen [26]. Using interference techniques, the complex amplitude of the confocal signal can be extracted. The 3D CTF for confocal interference microscopy with equal (illumination and detection) lens apertures and a small pinhole has been presented previously [19]. For a single wavenumber k, the 3D CTF has the same form as the CTF for confocal microscopy [27,28]. The CTF cutoff is given by

$$K_x^2 + K_y^2 + K_z^2 = K^2 < 4k^2, -2k < K_z < -2k\cos\alpha, \qquad (2)$$

where α is the semiangle subtended by the lens. The behavior is very different from holography in that now a finite volume of K-space is imaged. For scanning correlation microscopy, there is no physical pinhole, but the reference beam wavefront acts as a synthetic pinhole [29,30]. This approach has usually been performed using a heterodyne scheme but can also be done using homodyne detection and phase shifting or other digital processing. Scanning correlation microscopy has the advantage over confocal microscopy that signal detection is more efficient. If the correlation signal is detected over a large detector area, the effective CTF is $P_1 \otimes (P_2 P_{\mathrm{ref}}^*)$, where P_{ref} is the reference beam pupil [25,30], which is identical to that in the confocal case if the reference pupil is sufficiently large.

4. OCT AND OCM

OCT [7] is basically a confocal interference microscope with an additional optical sectioning effect arising from the limited temporal coherence of the illuminating light. OCM [8] refers to a system using lenses of numerical aperture high enough that the confocal sectioning is appreciable. Thus, for each spectral component, the 3D CTF is identical to that in a confocal interference system of the same geometry. In conventional OCT, the apertures of the illuminating and collecting pupils (in practice from the same lens) are small and equal. If the aperture is small enough that we can neglect the contribution to longitudinal resolution from the confocal effect, the longitudinal resolution comes only from temporal coherence effects. This means that the 3D CTF for a single spectral component is simply $(P_1 \otimes_2 P_2)(K_x, K_y)\delta(K_z + 2k)$, where $\otimes_2$represents 2D convolution. Assuming the pupils to be fully filled circular apertures, as is normally the case in confocal microscopy, the 3D CTF for OCT has been presented elsewhere [19]. In practice, the lenses in OCT are usually not fully filled, and for a system using single-mode fiber-optic implementation, the pupils are equal and close to Gaussians. The fiber mode in this case acts as a synthetic pinhole in the detection process [31]. The CTF model has recently been applied to imaging in OCM [32]. The behavior of confocal microscopes with Gaussian pupils has also been previously explored in depth [33,34]. In the paraxial approximation the CTF is very simple [31,34,35]:

$$c(\mathbf{K}) = \exp(-AK_z),$$
$$K_x^2 + K_y^2 + K_z^2 = K^2 \le 4k^2 \;\&\; K_z < 0, \qquad (3)$$

where A is a constant that depends on the width of the Gaussian pupil, i.e., on the fiber spot size and the geometry, and we have retained the spherical form of the cutoff rather than approximating it to a paraboloid. Again the CTF for a single wavelength is nonzero over a finite volume of K-space. It is noted that, for constant K_x, K_y, the CTF has a maximum value on the spherical boundary

$$K_z = -\sqrt{4k^2 - K_x^2 - K_y^2}. \qquad (4)$$

After performing a 2D Fourier transform of a single transverse image, we can map on to the surface of the sphere, assuming that the signal comes from this particular value of K_z. We note also that the spatial frequencies for a single wavelength do not all lie on the surface of the sphere. Assuming they do is equivalent to assuming that the major contribution to the scattering comes from exact backscattering (i.e., light scattered back in the direction from which it came). We recognize the similarity of exact backscattering with synthetic aperture nondestructive testing, where the sample is scanned by a point source and a point detector scanned in unison (like unistatic radar), so that, in the synthetic aperture case, true exact backscattering is indeed recorded [36]. Once the information from a single wavelength is mapped on to the sphere, using a spread of wavelengths, a 3D image can be reconstructed in a similar way to digital holographic reconstruction, except that the scattering data are assumed to lie on the sphere $K = 2$ [Eq. (5)] rather than the Ewald sphere, which passes through the origin [Eq. (2)] [17,20]. This is the method of ISAM. Taking a smaller value for A increases the lateral resolution but also increases the confocal sectioning, thus decreasing the longitudinal depth of field.

Equation (5) gives the locus of the maximum of the CTF, which is the same as is used in published papers on ISAM. But a more accurate reconstruction would result by approximating the CTF to its mean position rather than its maximum (the mode). From Eq. (3), we see that this simply translates the sphere axially so that

$$K_z = \frac{1}{\sqrt{\pi A}} - \sqrt{4k^2 - K_x^2 - K_y^2}. \qquad (5)$$

As the final step of the ISAM reconstruction is to find the modulus of the scattering potential, which is also equivalent to a shift of the sphere, the additional term in Eq. (4) cancels out. OCT usually uses only a moderate value for the numerical aperture, but if a nonparaxial theory is applied, we would expect that it could result in a small deformation of the sphere rather than a simple shift. Based on the scalar

complex-source point (CSP) theory of nonparaxial Gaussian beams for simplicity, the pupil function for a wavenumber k is

$$P(\mathbf{K}) = \exp[-B(k + K_z)], \qquad K = k, \tag{6}$$

where B is a constant [37,38]. Then the CTF can be calculated analytically as [28]

$$c(\mathbf{K}) = \frac{2k}{K} \exp[-B(2k + K_z)], \qquad K \le 2k, \tag{7}$$

which is shown in Fig. 1 for $B = 2$. The factor $1/K$ results from the angle of intersection of the two spherical shells when calculating the convolution and distorts the exponential dependence on K_z. For a system satisfying the sine condition,

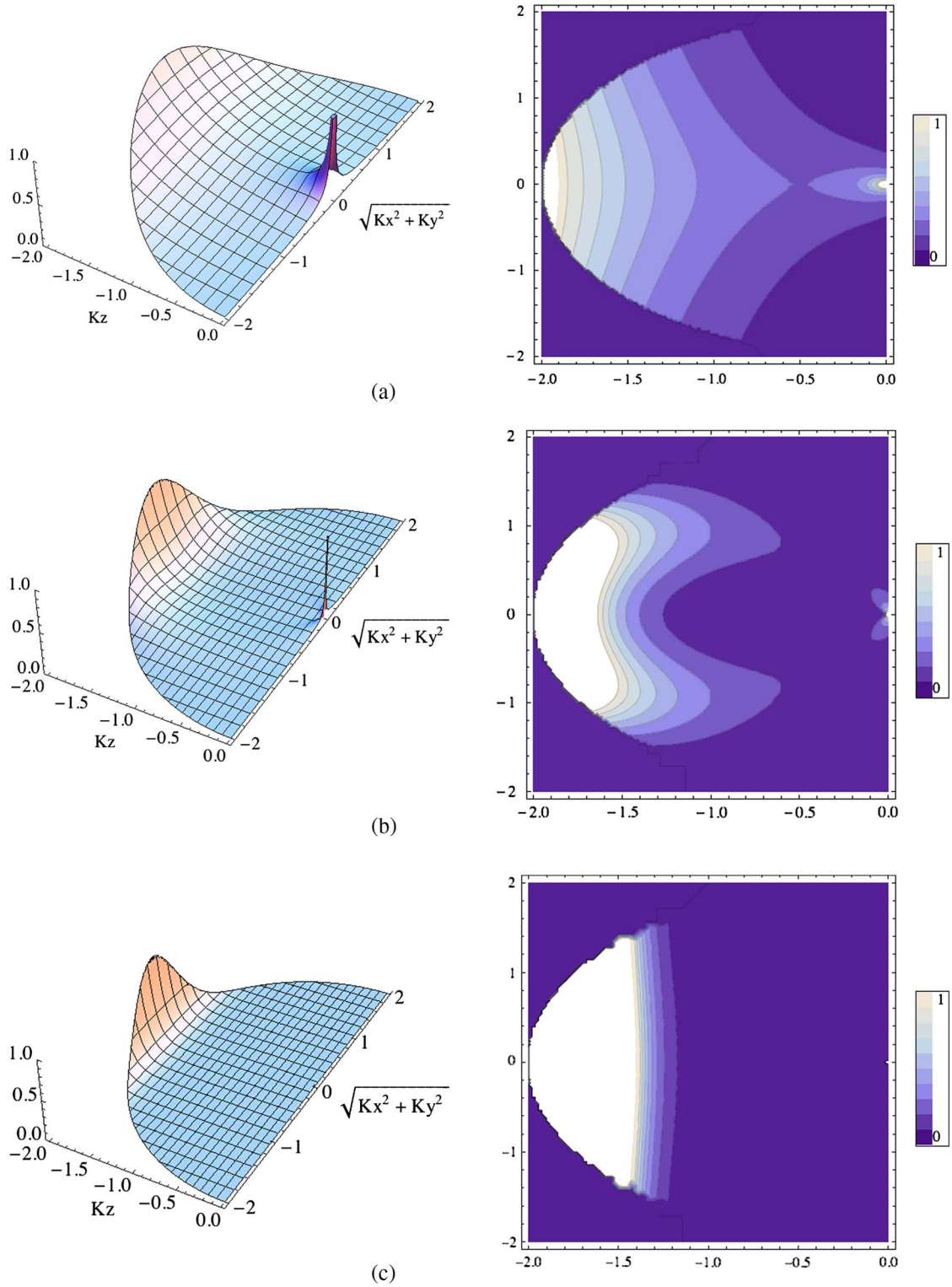

Fig. 1. (Color online) CTF and its contour plot for a CSP Gaussian beam: (a) $B = 2$, (b) $B_1 = 20$, $B_2 = 2$, (c) $B_1 = B_2 = 11$.

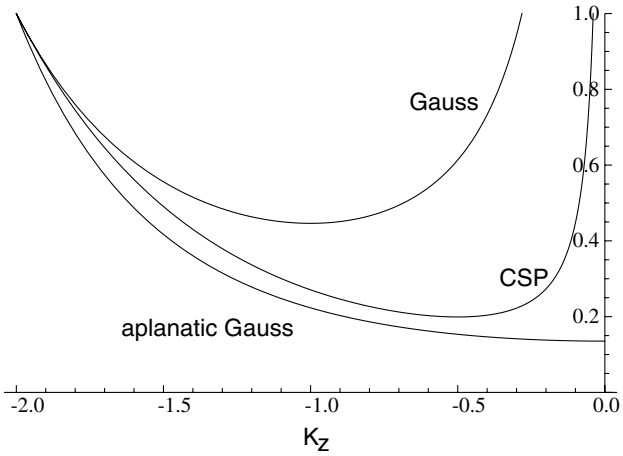

Fig. 2. Comparison of three different Gaussian beam models for $B = 2$: CSP model, a Gaussian beam focused by an aplanatic lens, and a Gaussian beam focused without aplanatic weighting.

this $1/K$ factor tends to cancel with the aplanatic factor. For example, for a different, and more realistic, model for a nonparaxial Gaussian, that of a Gaussian beam focused by an aplanatic lens, the pupil function is $P(\mathbf{K}) = (-K_z)^{1/2} \exp[-B(k^2 - K_z^2)/2]$. The general CTF cannot be expressed analytically, but for $K_x = K_y = 0$ it is given by

$$c(K_z) = \exp[-B(4k^2 - K_z^2)/4] \tag{8}$$

and is shown in Fig. 2. The behavior of a focused Gaussian beam without the aplanatic weighting is also shown and compared with the CSP solution. Figure 3 shows cross sections through the CTF at a constant value of $(K_x^2 + K_y^2)^{1/2}$ for a Gaussian beam focused by an aplanatic lens, assuming the angle of cutoff of the pupil is a full 90°, illustrating that the shapes of the cross sections vary.

ISAM uses exactly the same hardware as in normal spectral domain OCT, and the novelty is in the image reconstruction, which resembles holographic image reconstruction. We note that the ISAM papers do not mention specifically the 3D CTF framework. In particular, in [1], Eq. (3.17*a*) is the defocused 2D CTF (the Fourier transform of the 3D CTF). The defocused 2D pupil is given in Eq. (3.5) and is assumed to be equal for illumination and detection [Eq. (3.17*b*)]. The signal is reconstructed in the spatial z domain. In [2], Eq. (5) gives the signal spectrum in terms of the 2D CTF. This is evaluated by an asymptotic method for large values of π/NA and Gaussian-weighted pupils, giving in their Eq. (9) the signal spectrum as the product of the scattering potential and other terms that in fact are equivalent to the 3D CTF.

An advantage of the presented generic model based on the 3D CTF is that we can explore the behavior of different system configurations and can look at the effect of different pupils. For example, if the illumination is a CSP Gaussian with parameter B_1 in Eq. (7), while the reference beam is a CSP Gaussian with parameter B_2, $B_2 \le B_1$, the CTF is

$$c(\mathbf{K}) = \frac{2k}{K} I_0\left[(B_2 - B_1)\frac{\sqrt{K_x^2 + K_y^2}}{K}\sqrt{1 - \frac{K^2}{4}}\right] \exp\left[-(B_1 + B_2)\left(k + \frac{K_z}{2}\right)\right], \tag{9}$$

$$K \le 2k,$$

where I_0 is a modified Bessel function. The behavior is shown in Figs. 1 and 3 for $B_2 = 2$, $B_1 = 10$ or 20. As B_1 increases for constant B_2, the width of the CTF in the K_z direction decreases, making the approximation of fixed K_z for a given K_x, K_y better. The transverse resolution also decreases. But an important observation is that the CTF does not necessarily lie on the backscattering sphere of Eq. (5). Indeed, we know that, for large B_1, the system degenerates to DHM, for which the CTF is the Ewald sphere given by Eq. (2). In fact Eq. (9) represents the CTF for holographic microscopy for a coherent focused Gaussian illumination. Any combination of B_1 and B_2, such that $B_1 + B_2$ is constant, results in similar transverse resolution and depth of focus. But the locus of K_z for the maximum value of the CTF as a function of K_x, K_y is different. Thus, MWDHM could prove equally as suitable as OCM as a basis for implementation of ISAM, using an appropriate reconstruction algorithm [based on Eq. (2)].

The 3D CTF for a scalar aplanatic system of high aperture has been presented previously [28]. The form is similar to that for a Gaussian-weighted pupil. But without the aplanatic weighting, i.e., for a uniform spherical wave, the system

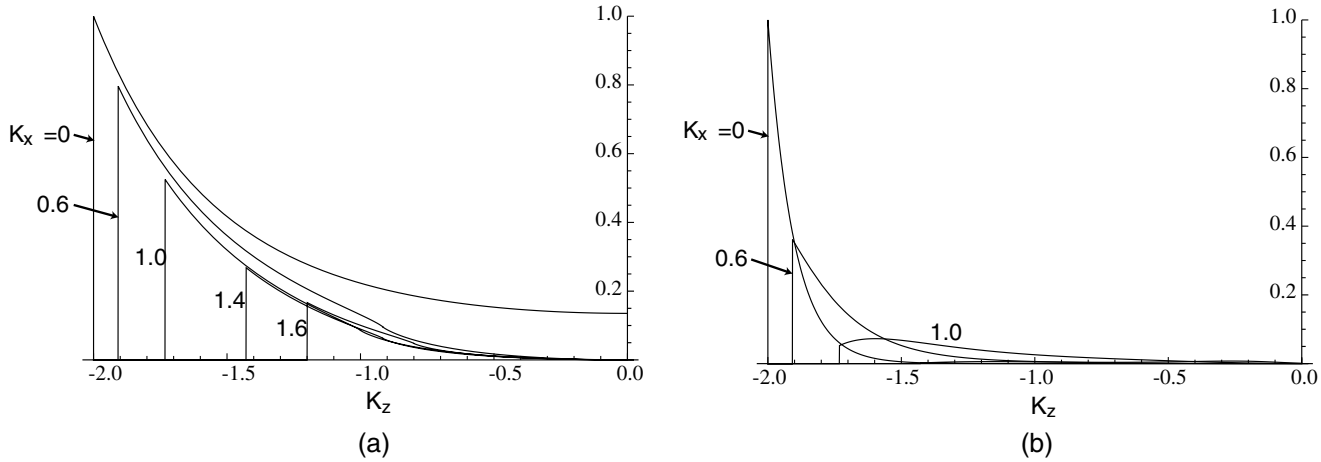

Fig. 3. Cross sections through the CTF for $K_y = 0$ for (a) a Gaussian beam focused by an aplanatic lens, $B = 2$, (b) for CSP Gaussian beams $B_1 = 20$, $B_2 = 2$.

behaves quite differently. For constant K_x, K_y the CTF has a maximum value on a toroidal surface

$$K_z = -k\cos\alpha - \sqrt{k^2\cos^2\alpha + 2kK_\rho - K_\rho^2}, \qquad (10)$$

where $K_\rho = K_x^2 + K_y^2$, rather than a sphere. It is also interesting to note that an OCT system with annular pupils can give a CTF that exhibits a maximum on a plane of constant K_z [39], so that this optical arrangement might prove desirable when using the standard, simple, OCT reconstruction algorithm. The effect on the CTF of using Bessel beams in an OCM system has also been recently investigated [32]. Use of a Bessel beam together with a circular collection pupil in confocal microscopy has been investigated extensively [40–42]. The CTF is nonzero only on the toroidal surface of Eq. (10), where α is the angle of propagation of the Bessel beam.

In [6], the figure shows a free-space optical system, i.e., without optical fibers. It is not clear if this was just for artistic impression or the implementation used, but nevertheless we now investigate briefly free-space systems, as in FFOCT [9]. For illumination by a Gaussian beam, the illuminating pupil is Gaussian, so the effect is similar to using a fiber. For the detection side, the behavior depends on the geometry of the detector. If the detector pixel size is small (i.e., if using a line CCD if the width of the device is small compared with the size of the focused spot on the detector), the system behaves as a confocal system, so the collection pupil has no Gaussian weighting, and its aperture could also be designed to be larger than the illumination pupil to improve overall transverse resolution. If, on the other hand, the pixel size is large, the system is a correlation microscope, and the collection pupil is weighted by the pupil of the reference beam P_{ref} [25,30]. In this latter case, imaging can be made to be identical to the fiber-based system, for an appropriate geometry.

5. SCATTERING POTENTIAL

Wolf analyzed the forward-scattered light in holography based on the first Born approximation [18]. The scattering object is described by the scattering potential

$$F(\mathbf{r}) = -k_0^2[n^2(\mathbf{r}) - 1], \qquad (11)$$

where k_0 is the free-space wavenumber. The quantity $[n^2(\mathbf{r}) - 1]$ has been recognized as the electric susceptibility of the sample. However, the Born approximation is known to be valid only for very small changes in refractive index, so a more accurate reconstruction is achieved if the changes in refractive index are measured relative to the background refractive index n_B rather than that of free space, to give a scattering potential

$$F(\mathbf{r}) = -k_0^2[n^2(\mathbf{r}) - n_B^2] = -k_B^2\{[n^2(\mathbf{r})/n_B^2] - 1\}. \qquad (12)$$

A constant background, of course, gives only a delta function in K-space so does not affect the final reconstruction apart from a constant refractive index term. However, in many application areas, including surface scattering [43], thin film optics [44,45], and seismic imaging [46], it has been recognized that the Born approximation is not accurate for backward scattering and that a model based on the Kirchhoff approximation is preferable. Basically, the Kirchhoff approximation

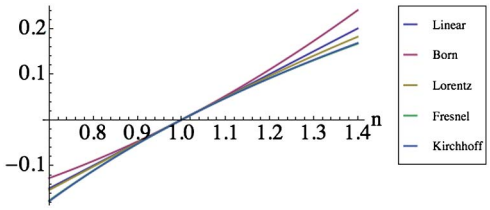

Fig. 4. (Color online) Variation of various functions of refractive index: $\frac{1}{2}(n-1)$ (linear), $\frac{1}{4}(n^2-1)$ (Born), $\frac{3}{4}(n^2-1)/(n^2+2)$ (Lorentz), $(n-1)/(n+1)$ (Fresnel), and $\frac{1}{2}\ln n$ (Kirchhoff).

shows that scattering occurs because of *changes* in refractive index rather than resulting from the refractive index itself [47–49]. According to this theory, the scattering potential is of the form

$$F(\mathbf{r}) \propto \frac{1}{2}\nabla^2 \ln\left(\frac{n(\mathbf{r})}{n_B}\right). \qquad (13)$$

This is seen to vanish in a region of constant refractive index, and choice of n_B does not affect the value of the scattering potential. This scattering potential differs from that in the Born approximation in two ways. First, the logarithm gives a very good approximation to the Fresnel reflection coefficient for normal incidence, $(n - n_B)/(n + n_B)$. These two forms are compared in Fig. 4 for the case $n_B = 1$. The logarithmic form is also a good approximation to the rigorous prediction for scattering by a small sphere given by Lorentz, $\frac{3}{4}(n^2-1)/(n^2+2)$, which has been shown to give an improved form of scattering potential for large permittivity [50]. All expressions have been normalized so that they agree with the Fresnel reflection coefficient for small refractive index changes. The second difference is that, as a result of the ∇^2 in Eq. (13), in K-space the object spectrum is weighted by a factor K^2. This factor results from the fact that the reflection coefficient is coherently averaged over s and p polarizations. Note that this average is performed on reflection coefficients whose signs are defined so that s and p give the same value of reflection coefficient for normal incidence, which is not the usual convention for the Fresnel coefficients [48]. The factor K just becomes a constant 2 either for exact backscattering or in the small aperture limit. So it has no effect on the normal ISAM reconstruction but could alter the alternative strategies mentioned above.

6. CONCLUSIONS AND DISCUSSION

It is argued that the hardware of ISAM is based on conventional spectral domain interferometry with a reconstruction algorithm that assumes that exact backscattering dominates. The algorithm has been justified using a theory based on the principle of the 3D CTF. Alternative algorithms could be superior for modified optical systems.

We finish with a discussion on the differences between OCT, OCM, and ISAM. Villiger and Lasser [32] comment that our earlier paper [19] did not discuss "the specific effects of frequency-domain OCT, because it considered a time-domain system." However, it can be seen that [19] makes the point that OCT imaging for a particular wavelength is identical with that in a confocal system, for which the CTF is given in [27,31] and can be directly applied to frequency-domain OCT. In addition, Fig. 7 of [19] shows the overall CTF for OCT with a

broadband source, neglecting the optical sectioning effect of the confocal gating, which is the same for either time- or frequency-domain systems. Reference [19] also says "these CTFs will be spread out in the low-coherence case, in a way similar to that in imaging with ultrashort pulses." The CTF for ultrashort pulsed imaging was presented by Gu and Sheppard [51] and is the convolution of the 3D CTF with the spectral distribution. It is again valid for both time- and frequency-domain systems but only if the object is scanned relative to the objective lens to generate a 3D image. This stresses a major difference between OCT and OCM: frequency-domain OCM requires information to be recorded as function of both defocus and wavelength, as otherwise 3D image formation is space variant. In ISAM, defocus information is not recorded, and hence the 3D reconstruction, while being superior to standard OCT reconstruction, is necessarily approximate.

REFERENCES

1. T. S. Ralston, D. L. Marks, P. S. Carney, and S. A. Boppart, "Inverse scattering for optical coherence tomography," J. Opt. Soc. Am. A **23**, 1027–1037 (2006).
2. T. S. Ralston, D. L. Marks, P. S. Carney, and S. A. Boppart, "Interferometric synthetic aperture microscopy," Nat. Phys. **3**, 129–134 (2007).
3. D. L. Marks, T. S. Ralston, S. A. Boppart, and P. S. Carney, "Inverse scattering for frequency-scanned full-field optical coherence tomography," J. Opt. Soc. Am. A **24**, 1034–1041 (2007).
4. B. J. Davis, T. S. Ralston, D. L. Marks, S. A. Boppart, and P. S. Carney, "Autocorrelation artifacts in optical coherence tomography and interferometric synthetic aperture microscopy," Opt. Lett. **32**, 1441–1443 (2007).
5. B. J. Davis, S. Schlachter, D. L. Marks, T. S. Ralston, S. A. Boppart, and P. S. Carney, "Non-paraxial vector-field modeling of optical coherence tomography and interferometric synthetic aperture microscopy," J. Opt. Soc. Am. A **24**, 2527–2542 (2007).
6. T. S. Ralston, G. L. Charvat, S. G. Adie, B. J. Davis, P. S. Carney, and S. A. Boppart, "Microscopic laser radar," Opt. Photon. News **21**(6), 32–38 (2010).
7. D. Huang, E. A. Swanson, C. P. Lin, J. S. Schuman, W. G. Stinson, W. Chang, M. R. Lee, T. Flotte, K. Gregory, C. A. Puliafito, and J. G. Fujimoto, "Optical coherence tomography," Science **254**, 1178–1181 (1991).
8. J. A. Izatt, M. R. Hee, G. M. Owen, E. A. Swanson, and J. G. Fujimoto, "Optical coherence microscopy in scattering media," Opt. Lett. **19**, 590–592 (1994).
9. A. Dubois, L. Vabre, A.-C. Boccara, and E. Beaurepaire, "High-resolution full-field optical coherence tomography with a Linnik microscope," Appl. Opt. **41**, 805–812 (2002).
10. M. Roy and C. J. R. Sheppard, "Geometric phase-shifting for low-coherence interference microscopy," Opt. Lasers Eng. **37**, 631–641 (2002).
11. M. Roy, C. J. R. Sheppard, and P. Hariharan, "Low-coherence interference microscopy using a ferro-electric liquid crystal phase-modulator," Opt. Express **12**, 2512–2516 (2004).
12. D. K. Hamilton and C. J. R. Sheppard, "A confocal interference microscope," Opt. Acta **29**, 1573–1577 (1982).
13. E. Cuche, F. Bevilacqua, and C. Depeursinge, "Digital holography for quantitative phase-contrast imaging," Opt. Lett. **24**, 291–293 (1999).
14. V. Lauer, "New approach to optical diffraction tomography yielding a vector equation of diffraction tomography and a novel tomographic microscope," J. Microsc. **205**, 165–176 (2002).
15. F. Charrière, M. A. F. Montfort, J. Kühn, T. Colomb, E. Cuche, P. Marquet, and C. Depeursinge, "Cell refractive index tomography by digital holographic microscopy," Opt. Lett. **31**, 178–180 (2006).
16. W. Choi, C. Fang-Yen, K. Badizadegan, R. R. Dasari, and M. S. Feld, "Extended depth of focus in tomographic phase microscopy using a propagation algorithm," Opt. Lett. **33**, 171–173 (2008).
17. J. Kuehn, F. Montfort, T. Colomb, B. Rappaz, C. Moratal, N. Pavillon, P. Marquet, and C. Depeursinge, "Submicrometer tomography of cells by multiple wavelength digital holographic microscopy in reflection," Opt. Lett. **34**, 653–655 (2009).
18. E. Wolf, "Three-dimensional structure determination of semi-transparent objects from holographic data," Opt. Commun. **1**, 153–156 (1969).
19. C. J. R. Sheppard, M. Roy, and M. D. Sharma, "Image formation in low-coherence and confocal interference microscopes," Appl. Opt. **43**, 1493–1502 (2004).
20. S. S. Kou and C. J. R. Sheppard, "Imaging in digital holographic microscopy," Opt. Express **15**, 13640–13648 (2007).
21. R. Dändliker and K. Weiss, "Reconstruction of the three-dimensional refractive index from scattered waves," Opt. Commun. **1**, 323–328 (1970).
22. C. J. R. Sheppard, "The spatial frequency cut-off in three-dimensional imaging," Optik **72**, 131–133 (1986).
23. C. J. R. Sheppard and C. J. Cogswell, "Three-dimensional image formation in confocal microscopy," J. Microsc. **159**, 179–194 (1990).
24. C. J. R. Sheppard and C. J. Cogswell, "Three-dimensional imaging in confocal microscopy," in *Confocal Microscopy*, T. Wilson, ed. (Academic, 1990), pp. 143–169.
25. C. J. R. Sheppard and T. Wilson, "Fourier imaging of phase information in conventional and scanning microscopes," Phil. Trans. R. Soc. A **295**, 513–536 (1980).
26. C. W. McCutchen, "Generalized aperture and the three-dimensional diffraction image," J. Opt. Soc. Am. **54**, 240–244 (1964).
27. C. J. R. Sheppard, M. Gu, and X. Q. Mao, "Three-dimensional coherent transfer function in a reflection-mode confocal scanning microscope," Opt. Commun. **81**, 281–284 (1991).
28. C. J. R. Sheppard, M. Gu, Y. Kawata, and S. Kawata, "Three-dimensional transfer functions for high aperture systems," J. Opt. Soc. Am. A **11**, 593–598 (1994).
29. T. Sawatari, "Optical heterodyne scanning microscope," Appl. Opt. **12**, 2768–2772 (1973).
30. M. Kempe and W. Rudolf, "Comparative study of confocal and heterodyne microscopy for imaging through scattering media," J. Opt. Soc. Am. A **13**, 46–52 (1996).
31. M. Gu, X. Gan, and C. J. R. Sheppard, "Three-dimensional coherent transfer functions in fibre optical confocal scanning microscopes," J. Opt. Soc. Am. A **8**, 1019–1025 (1991).
32. M. Villiger and T. Lasser, "Image formation and tomogram reconstruction in optical coherence microscopy," J. Opt. Soc. Am. A **27**, 2216–2228 (2010).
33. C. J. R. Sheppard and T. Wilson, "The theory of scanning microscopes with Gaussian pupil functions," J. Microsc. **114**, 179–197 (1978).
34. C. J. R. Sheppard, H. Fatemi, and M. Gu, "The Fourier optics of near-field microscopy," Scanning **17**, 28–40 (1995).
35. M. Gu and C. J. R. Sheppard, "Fibre-optical confocal scanning interference microscopy," Opt. Commun. **100**, 79–86 (1993).
36. G. S. Kino, "Acoustic imaging for nondestructive evaluation," Proc. IEEE **67**, 510–525 (1979).
37. G. A. Deschamps, "Gaussian beam as a bundle of complex rays," Electron. Lett. **7**, 684–685 (1971).
38. C. J. R. Sheppard and S. Saghafi, "Beam modes beyond the paraxial approximation: a scalar treatment," Phys. Rev. A **57**, 2971–2979 (1998).
39. M. Gu and C. J. R. Sheppard, "Three-dimensional coherent transfer functions in confocal imaging with two unequal annular lenses," J. Mod. Opt. **40**, 1255–1272 (1993).
40. C. J. R. Sheppard, "The use of lenses with annular aperture in scanning optical microscopy," Optik **48**, 329–334 (1977).
41. C. J. R. Sheppard and A. Choudhury, "Image formation in the scanning microscope," Opt. Acta **24**, 1051–1073 (1977).
42. C. J. R. Sheppard and T. Wilson, "Imaging properties of annular lenses," Appl. Opt. **18**, 3764–3769 (1979).
43. R. J. Wombell and J. A. De Santo, "Reconstruction of rough-surface profiles with the Kirchhoff approximation," J. Opt. Soc. Am. A**8**, 1892–1897 (1991).
44. C. H. Greenewalt, W. Brandt, and D. D. Friel, "Irridescent colors of hummingbird feathers," J. Opt. Soc. Am. **50**, 1005–1013 (1960).

45. C. J. R. Sheppard, "Approximate calculation of the reflection coefficient from a stratified medium," Pure Appl. Opt. **4**, 665–669 (1995).
46. L. M. Brekhovskikh, *Waves in Layered Media* (Academic, 1960).
47. C. J. R. Sheppard, T. J. Connolly, and M. Gu, "The scattering potential for imaging in the reflection geometry," Opt. Commun. **117**, 16–19 (1995).
48. C. J. R. Sheppard and F. Aguilar, "Fresnel coefficients for weak reflection and the scattering potential for three-dimensional imaging," Opt. Commun. **162**, 182–186 (1999).
49. C. J. R. Sheppard, "Scattering and the spatial frequency representation," in *Light Scattering and Nanoscale Surface Roughness*, A. A. Maradudin, ed. (Springer, 2007), pp. 61–92.
50. P. C. Chaumet, A. Sentenac, and A. Rahmani, "Coupled dipole method for scatterers with large permittivity," Phys. Rev. E **70**, 036606 (2004).
51. M. Gu and C. J. R. Sheppard, "Three-dimensional image formation in confocal microscopy under ultra-short laser-pulse illumination," J. Mod. Opt. **42**, 747–762 (1995).